

Faraday resonance in dynamical bar instability of differentially rotating stars

Motoyuki Saijo*

School of Mathematics, University of Southampton, Southampton SO17 1BJ, United Kingdom

Yasufumi Kojima†

Department of Physics, Hiroshima University, Higashi-Hiroshima 739-8526, Japan

(Received 7 August 2007; Revised 11 January 2008; Accepted 11 February 2008)

We investigate the nonlinear behaviour of the dynamically unstable rotating star for the bar mode by three-dimensional hydrodynamics in Newtonian gravity. We find that an oscillation along the rotation axis is induced throughout the growth of the unstable bar mode, and that its characteristic frequency is twice as that of the bar mode, which oscillates mainly along the equatorial plane. A possibility to observe Faraday resonance in gravitational waves is demonstrated and discussed.

PACS numbers: 97.10.Kc, 04.25.D-, 04.30.Db, 95.30.Lz

I. INTRODUCTION

Parametric resonance is widely observed in hydrodynamics, nonlinear optics, chemical reaction and classical oscillatory systems. It is also interesting from the bifurcation theory and the pattern formation. The scientific study in the fluid mechanics dates from the experiments by Faraday in 1831, and is therefore named Faraday resonance (e.g., [1]). Nonlinear dynamics exhibits mode interaction of oscillation in different direction, and possibly causes the resonant growth of a particular mode. Recently, experimental studies of Faraday resonance demonstrate that the system of fluid mechanics [2] and that of Bose-Einstein condensate [3] work perfectly. These agreements in different fields also suggest that Faraday resonance may also occur in an astrophysical context. Quasi-periodic oscillation in gravitational waves from dynamical/secular instabilities is expected to be excited throughout rotating core collapse, and may drive resonant growth.

Dynamical bar instability in a rotating equilibrium star takes place when the ratio β ($\equiv T/W$) between rotational kinetic energy T and the gravitational binding energy W exceeds the critical value β_{dyn} (≈ 0.27 for an uniformly rotating incompressible body in Newtonian gravity [4]). Determining the onset of the dynamical bar-mode instability, as well as the subsequent evolution of an unstable star, requires a fully nonlinear hydrodynamic simulation. Simulations performed in Newtonian gravity (e.g., [5, 6, 7, 8, 9, 10, 11, 12, 13, 14]) have shown that β_{dyn} depends very weakly on the stiffness of the equation of state. β_{dyn} becomes small for stars with high degree of differential rotation [15, 16, 17]. Simulations in relativistic gravitation [18, 19, 20] have shown that β_{dyn} decreases when increases the compactness of the star, indicating that relativistic gravitation enhances the bar-mode instability. Recent numerical simulations show that dy-

namical bar instability can occur at significantly lower β than the threshold $\beta_{\text{crit}} \approx 0.27$ [17, 22, 23, 24, 25]. These recent findings can be classified into the category of a low T/W dynamical instability. This instability may be triggered by the corotation resonance [26, 27], which is completely different from the standard dynamical bar-mode instability triggered by a certain magnitude of rotation [4, 28, 29].

Our main concern in this paper is not to determine the onset of the instability, but to study the dynamical features of the bar. For this purpose, we numerically study the growing behaviour of the azimuthal modes in the nonlinear regime for a longer timescale. One interesting issue of nonlinear evolution is the possibility of resonant growth of other azimuthal modes triggered by the dynamical bar-mode instability. One candidate for such resonance is Faraday resonance, which is excited by the external periodic force. According to the linear approximation of the velocity potential by using an incompressible inviscid liquid in a rectangular tank, the time-dependent behaviour of the liquid surface is expressed by the Mathieu's equation (e.g., [30]). The dynamically unstable bar mode may work for other azimuthal oscillation modes as an external periodic force. The oscillation is not exactly periodic, but rather quasi-periodic, and may trigger a parametric resonance.

The other interesting issue of nonlinear evolution is the duration of the bar shape, when it forms. This is quite important for gravitational wave detection. We basically believe that once the dynamical bar instability takes place, the system generates quasi-periodic gravitational waves for a period sufficient enough to be detected in the ground-based gravitational wave detectors. The only causes to destruct a bar are dissipative effects such as viscosity and gravitational radiation. The typical timescale of such effects takes place in the secular timescale, which is much longer than the dynamical one of the system. Therefore the standard picture is that the bar can persist in its shape until the secular timescale. However, recent numerical simulation shows that a bar destructs its shape in the dynamical timescale [20]. The authors argue a possible cause of the destruction of bar as

*Electronic address: msl@maths.soton.ac.uk

†Electronic address: kojima@theo.phys.sci.hiroshima-u.ac.jp

azimuthal mode coupling. Although there was in the past a debate between the two numerical simulations about the persistence of a bar [12, 31], the different outcomes were considered as the different accuracy level of the center of mass condition at that time. Since there is the only one group that claims the destruction of bar structure in the dynamical timescale with a satisfaction of the center of mass condition, it is worth investigating the destruction of a bar employing a different computational code. In order to focus on this topic, it is sufficient to investigate this topic in three-dimensional hydrodynamics in Newtonian gravity.

This paper is organized as follows. In Sec. II we present the basic equations of our hydrodynamic simulation in Newtonian gravity. In Sec. III are discussed the numerical results of our findings of Faraday resonance. In Sec. IV we briefly summarize our findings. Throughout this paper, we use the geometrized units with $G = c = 1$ [36] and adopt Cartesian coordinates (x, y, z) with the coordinate time t . Note that Latin index takes (x, y, z) .

II. BASIC EQUATIONS

A. Newtonian Hydrodynamics

We construct a three dimensional Newtonian hydrodynamics code assuming an adiabatic Γ -law equation of state

$$P = (\Gamma - 1)\rho\varepsilon, \quad (2.1)$$

where P is the pressure, Γ the adiabatic index, ρ the mass density and ε the specific internal energy density. For perfect fluids the Newtonian equations of hydrodynamics consist of the continuity equation

$$\frac{\partial\rho}{\partial t} + \frac{\partial(\rho v^i)}{\partial x^i} = 0, \quad (2.2)$$

the energy equation

$$\frac{\partial e}{\partial t} + \frac{\partial(ev^j)}{\partial x^j} = -\frac{1}{\Gamma}e^{-(\Gamma-1)}P_{\text{vis}}\frac{\partial v^i}{\partial x^i}, \quad (2.3)$$

and the Euler equation

$$\frac{\partial(\rho v_i)}{\partial t} + \frac{\partial(\rho v_i v^j)}{\partial x^j} = -\frac{\partial(P + P_{\text{vis}})}{\partial x^i} - \rho\frac{\partial\Phi}{\partial x^i}. \quad (2.4)$$

Here v^i is the fluid velocity and Φ the gravitational potential; and e is defined according to

$$e = (\rho\varepsilon)^{1/\Gamma}. \quad (2.5)$$

We compute the artificial viscosity pressure P_{vis} from [32]

$$P_{\text{vis}} = \begin{cases} C_{\text{vis}}\rho(\delta v)^2, & \text{for } \delta v \leq 0; \\ 0, & \text{for } \delta v \geq 0, \end{cases} \quad (2.6)$$

where $\delta v \equiv 2\delta x\partial_i v^i$, $\delta x (= \Delta x = \Delta y = \Delta z)$ is the local grid spacing and where we choose the dimensionless parameter $C_{\text{vis}} = 2$. When evolving the above equations we limit the size Δt by an appropriately chosen Courant condition.

The gravitational potential is determined by the Poisson equation

$$\Delta\Phi = 4\pi\rho, \quad (2.7)$$

with the outer boundary condition

$$\Phi = -\frac{M}{r} - \frac{d_i x^i}{r^2} + O(r^{-3}). \quad (2.8)$$

Here M is the total mass

$$M = \int_V \rho dx^3 \quad (2.9)$$

and d_i is the dipole moment

$$d_i = \int_V \rho x_i dx^3. \quad (2.10)$$

B. Initial Data

As initial data, we construct differentially rotating equilibrium models with an algorithm based on Hachisu [33] and adopt cylindrical two dimensional coordinate to compute the axisymmetric equilibrium star. Individual models are parameterized by the ratio of the polar to equatorial radius R_p/R_{eq} , and a parameter of dimension length d that determines the degree of differential rotation through

$$\Omega = \frac{j_0}{d^2 + \varpi^2}. \quad (2.11)$$

Here Ω is the angular velocity, j_0 a constant parameter with units of specific angular momentum, and ϖ the cylindrical radius. The parameter d determines the length scale over which Ω changes; uniform rotation is achieved in the limit $d \rightarrow \infty$. For the construction of initial data we also assume a polytropic equation of state

$$P = \kappa\rho^{1+1/n}, \quad (2.12)$$

where $n = 1/(\Gamma - 1)$ is the polytropic index and κ a constant. In the absence of shocks, the polytropic form of the equation of state is conserved by the Γ -law equation of state (Eq. [2.1]).

We also compute the virial identity, which is identically zero in the equilibrium star, to show the accuracy level as

$$V_{\text{Nwt}} = \frac{|2T_{\text{tot}} - W + 3\Pi|}{W}, \quad (2.13)$$

where

$$T_{\text{tot}} = \frac{1}{2} \int \rho v^i v_i d^3x, \quad (2.14)$$

$$W = -\frac{1}{2} \int \rho \Phi d^3x, \quad (2.15)$$

$$\Pi = \int P d^3x. \quad (2.16)$$

Note that we have divided the value by a gravitational binding energy W so that the value V_{Nwt} is regarded as a relative error of the system. We summarize our four different rotating equilibrium stars in Table I.

C. Gravitational Waveforms

We compute approximate gravitational waveforms by evaluating the quadrupole formula. In the radiation zone, gravitational waves can be described by a transverse-traceless, perturbed metric h_{ij}^{TT} with respect to a flat spacetime. In the quadrupole formula, h_{ij}^{TT} is found from [34]

$$h_{ij}^{TT} = \frac{2}{r} \frac{d^2}{dt^2} I_{ij}^{TT}, \quad (2.17)$$

where r is the distance to the source, I_{ij} the quadrupole moment of the mass distribution (see Eq. [36.42b] in Ref. [34]), and where TT denotes the transverse-traceless projection. Choosing the direction of the wave propagation to be along the z -axis (rotational axis of the equilibrium star), we determine the two polarization modes of gravitational waves from

$$h_+^{(z)} \equiv \frac{1}{2}(h_{xx}^{TT} - h_{yy}^{TT}) \quad \text{and} \quad h_\times^{(z)} \equiv h_{xy}^{TT}. \quad (2.18)$$

For observers along the z -axis, we thus have

$$\frac{rh_+^{(z)}}{M} = \frac{1}{2M} \frac{d}{dt} (\dot{I}_{xx} - \dot{I}_{yy}), \quad (2.19)$$

$$\frac{rh_\times^{(z)}}{M} = \frac{1}{M} \frac{d}{dt} \dot{I}_{xy}. \quad (2.20)$$

Using the same procedure, the observers along the x -axis detect the wave propagates as

$$\frac{rh_+^{(x)}}{M} = \frac{1}{2M} \frac{d}{dt} (\dot{I}_{yy} - \dot{I}_{zz}), \quad (2.21)$$

$$\frac{rh_\times^{(x)}}{M} = \frac{1}{M} \frac{d}{dt} \dot{I}_{yz}. \quad (2.22)$$

The number of time derivatives I_{ij} that have to be taken out can be reduced by using the continuity equation (Eq. [2.2])

$$\dot{I}_{ij} = \int (\rho v^i x^j + \rho x^i v^j) d^3x, \quad (2.23)$$

in equations (2.19) – (2.22) (see Ref. [35]).

The spectrum of gravitational waveform can be computed as

$$S^{(x,z)} = |\tilde{h}_+^{(x,z)}|^2 + |\tilde{h}_\times^{(x,z)}|^2, \quad (2.24)$$

where

$$\tilde{h}_{+,\times}^{(x,z)} = \int dt h_{+,\times}^{(x,z)} e^{i\omega t}. \quad (2.25)$$

D. Diagnostics

We monitor the conservation of mass M (Eq. [2.9]), angular momentum J

$$J = \int \rho (xv^y - yv^x) d^3x, \quad (2.26)$$

and the location of the center of mass x_{CM}^i

$$x_{\text{CM}}^i = \int \rho x^i d^3x. \quad (2.27)$$

Due to our flux-conserving difference scheme the mass M is also conserved up to a round-off error, except if matter leaves the computational grid.

To monitor the development of the azimuthal modes ($m = 1, 2, 3, 4$) and the one in the z -direction, we compute the following five diagnostics

$$\begin{aligned} D &= \langle e^{im\varphi} \rangle_{m=1} \\ &= \frac{1}{M} \int \rho \frac{x + iy}{\sqrt{x^2 + y^2}} d^3x, \end{aligned} \quad (2.28)$$

$$\begin{aligned} Q &= \langle e^{im\varphi} \rangle_{m=2} \\ &= \frac{1}{M} \int \rho \frac{(x^2 - y^2) + i(2xy)}{x^2 + y^2} d^3x, \end{aligned} \quad (2.29)$$

$$\begin{aligned} O &= \langle e^{im\varphi} \rangle_{m=3} \\ &= \frac{1}{M} \int \rho \frac{x(x^2 - 3y^2) + iy(3x^2 - y^2)}{(x^2 + y^2)^{3/2}} d^3x, \end{aligned} \quad (2.30)$$

$$\begin{aligned} M_4 &= \langle e^{im\varphi} \rangle_{m=4} \\ &= \frac{1}{M} \int \rho \frac{(x^4 - 6x^2y^2 + y^4) + i(4x^2y^2(x^2 - y^2))}{(x^2 + y^2)^2} d^3x, \end{aligned} \quad (2.31)$$

$$D_z = \frac{1}{MR_p} \int \rho |z| d^3x, \quad (2.32)$$

where a bracket denotes the density weighted average. When we compute the four diagnostics in the equatorial plane ($D^{(\text{eq})}$, $Q^{(\text{eq})}$, $O^{(\text{eq})}$, $M_4^{(\text{eq})}$), we change the integral volume from d^3x to $dxdy$ and M to M_{eq} . Note that M_{eq} is the rest-mass density integrated only in the equatorial plane.

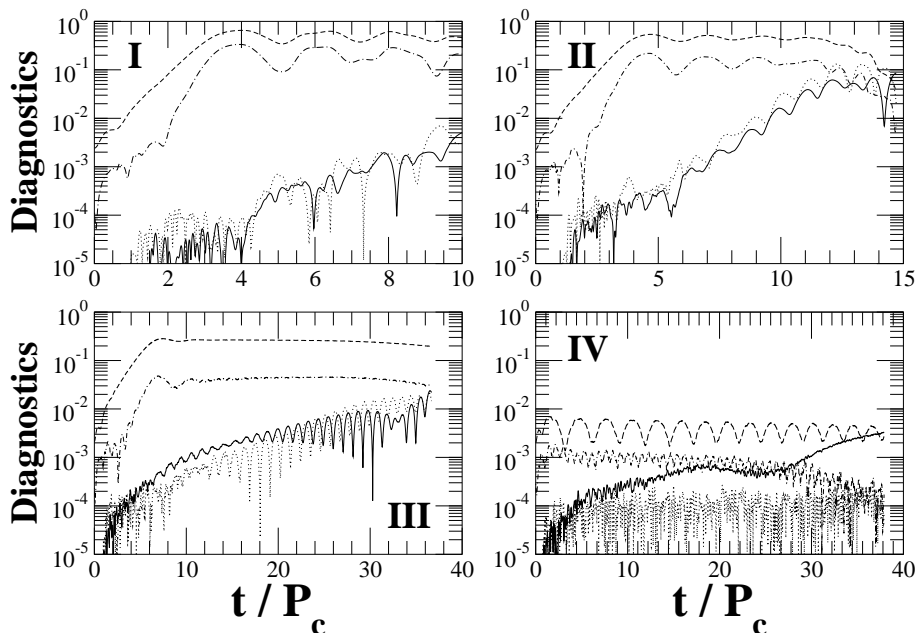


FIG. 1: Diagnostics $|D|$, $|Q|$, $|O|$, $|M_4|$ as a function of t/P_c for four different rotating stars (see Table I). Solid, dashed, dotted, and dash-dotted lines denote $|D|$, $|Q|$, $|O|$ and $|M_4|$, respectively. We terminate our simulation when the relative error of the rest mass exceeds $\sim 0.01\%$ for models I and II. Hereafter P_c represents the central rotation period at $t = 0$.

We also compute the spectra of the above five diagnostics as

$$|F_m|^2 = \left| \frac{1}{M} \int dt \int d^3x \rho e^{i(\omega t - m\varphi)} \right|^2 \quad (m = 1, \dots, 4), \quad (2.33)$$

$$|F_z|^2 = \left| \frac{1}{MR_p} \int dt \int d^3x |z| (\rho - \rho_{\text{avg}}) e^{i\omega t} \right|^2. \quad (2.34)$$

Since D_z does not oscillate around zero as we show later, we have subtracted the time averaged density ρ_{avg} from the original one to compute the spectrum. Note also that we have only integrated D_z in time after its first global maximum.

III. NUMERICAL RESULTS

Here we show our evolution of the differentially rotating stars. We terminate the integration when the relative error of the rest mass exceeds $\sim 10^{-4}$, since the only violation of the rest mass conservation is caused by the matter outflow at the outer boundary of computation. We also terminate the integration when the time exceeds $20 \sim 40$ central rotation periods, which are sufficient to enhance all m modes. Note that our code never crashes throughout the evolution.

To enhance any dynamically unstable mode, we disturb the initial equilibrium density ρ_{eq} by a non-axisymmetric perturbation according to [37]

$$\rho = \rho_{\text{eq}} \left[1 + \delta^{(2)} \frac{x^2 + 2xy - y^2}{R_{\text{eq}}^2} + \delta^{(4)} \frac{x^4 - 6x^2y^2 + y^4 + 4xy(x^2 - y^2)}{R_{\text{eq}}^4} \right], \quad (3.1)$$

where we set $\delta^{(2)} = \delta^{(4)} = 10^{-2}$.

We study four different differentially rotating stars, which are detailed in Table I to investigate the nonlinear behaviour of the non-axisymmetric dynamical bar instabilities. We choose the axis of rotation to align with the z axis, and assume planar symmetry across the equator. We choose the Cartesian coordinates with the computational grid points $401 \times 401 \times 101$ covering the equatorial

diameter of the equilibrium star as 121 grid points.

We show the amplitudes of our four diagnostics for all four models in Fig. 1. At the first stage of evolution, the $m = 2$ diagnostic grows exponentially in models I, II, and III, while it stays around the amplitude of $t = 0$ in model IV. Therefore the star of models I, II, and III is determined as dynamically unstable against bar mode, while that of model IV is stable. For the dynamically bar

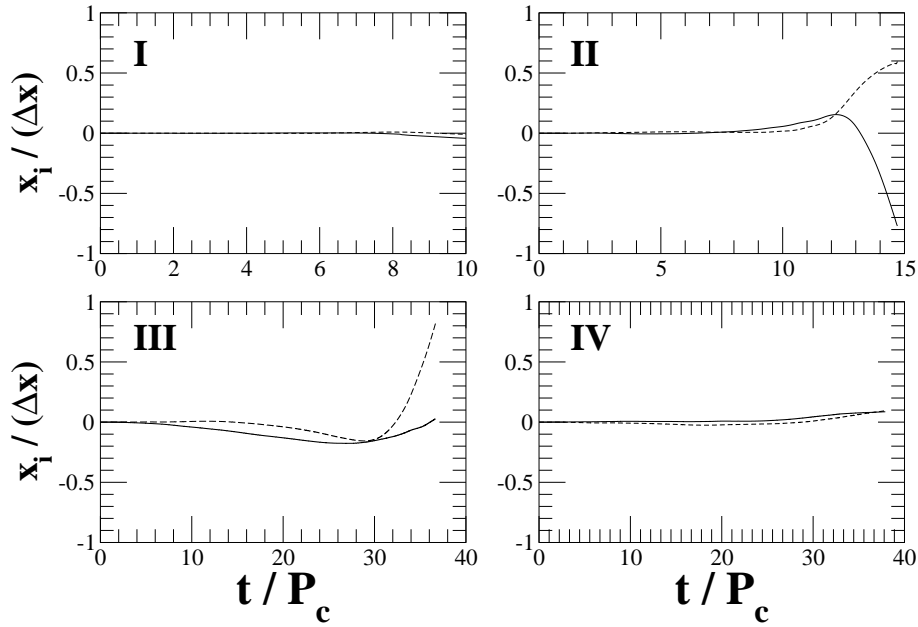


FIG. 2: Center of mass as a function of t/P_c . Solid, dashed line denotes the one of x and y direction, respectively.

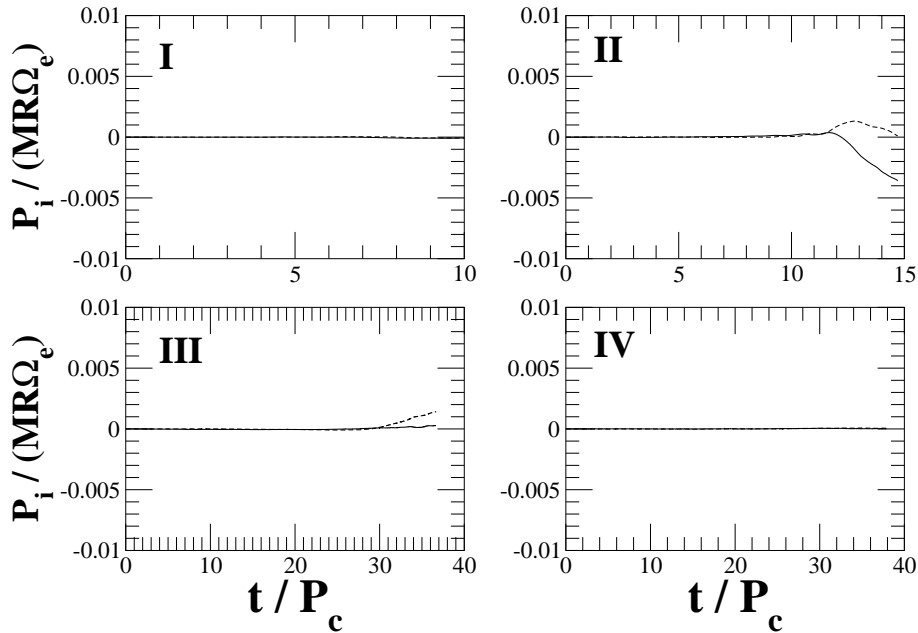


FIG. 3: Linear momentum as a function of t/P_c . Solid and dashed line denotes x and y component of the linear momentum, respectively. M and Ω_e represent the total rest-mass and the angular velocity at the equatorial surface at $t = 0$, respectively.

unstable stars (models I, II, and III), the $m = 2$ diagnostic grows exponentially but the other remaining m modes do not grow at the first evolution stage when imposing a small perturbation (Fig. 1). This result is consistent to the linear perturbation analysis of the dynamically bar unstable stars, which shows that the only dynamically unstable m mode is $m = 2$. Also the result confirms us that the amplitude of perturbation at $t = 0$ is adequate to treat the system linearly ($\delta^{(2)} \approx 10^{-2}$). After that stage

the $m = 4$ diagnostic grows exponentially because of the secondary harmonic of $m = 2$ mode, and then the odd m modes are also enhanced. The odd m modes are excited even if we do not impose the perturbation of their corresponding modes in the equilibrium star, since the finite differencing scheme always generates a small amount of all m modes (Fig. 1). However a small fluctuation at the wavefront should occur in nature so that the existence of all m modes, when the bar forms, are quite natural in

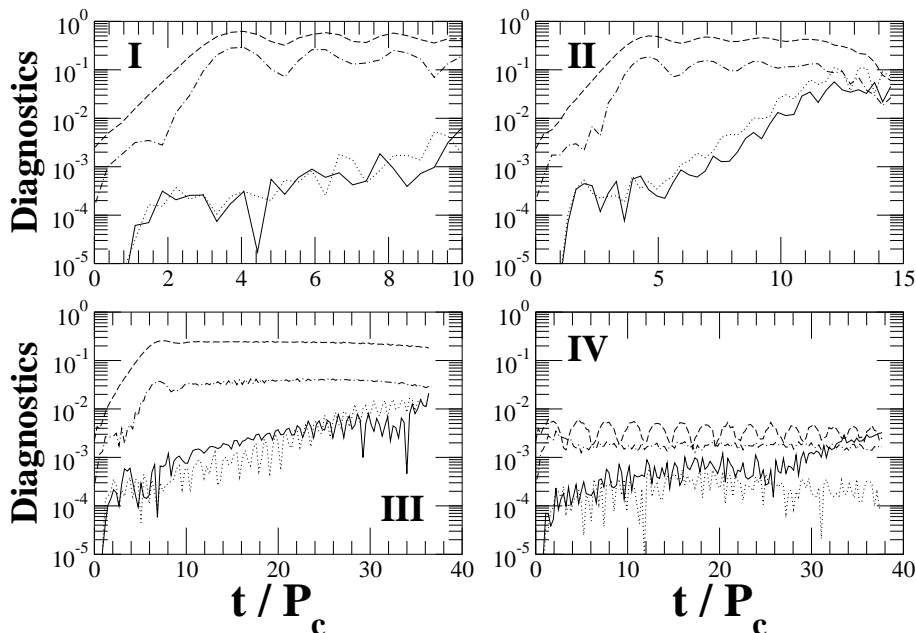


FIG. 4: Same as Fig. 1, but the diagnostics are only computed in the equatorial plane.

TABLE I: Four different rotating equilibrium stars in Newtonian gravity of $\Gamma = 2$, $d/R_{\text{eq}} = 1$.

Model	R_p/R_{eq}	T/W	V_{Ntw}
I	0.225	0.281	8.29×10^{-5}
II	0.250	0.277	8.79×10^{-5}
III	0.275	0.268	7.95×10^{-5}
IV	0.300	0.256	9.47×10^{-5}

reality.

We have monitored the center of mass and the linear momentum throughout the evolution to guarantee that we do not impose any additional physics in the system. Fig. 2 shows the center of mass of the four different stars throughout the evolution. We have confirmed that the numerical error only allows the star to change the center of mass within the one computational grid. We have also checked the linear momentum conservation in Fig. 3, which shows that the relative error is less than 1% of the total value constructed by the total mass and the velocity at the equilibrium equatorial surface. In order to check whether the center of mass condition significantly affects the diagnostics, we have also computed the following two types of diagnostics in the equatorial plane (e.g. [25]). One is the diagnostic with the same coordinate as in the simulation, while the other is the one with the coordinate where the center of mass is adjusted to zero in every snapshots. Since the equatorial diagnostic (Fig. 4) reproduces all characteristics of the one obtained from the three-dimensional computation (Fig. 1), the equatorial diagnostic may represent the three-dimensional one.

We compare Figs. 4 and 5, to focus on the effect of the center of mass condition on the diagnostics. For models I and II, the adjustment of the center of mass reduces the amplitude of $D^{(\text{eq})}$ and $O^{(\text{eq})}$ for $t \lesssim 5P_c$. However the condition does not change the exponential growth of $D^{(\text{eq})}$ and $O^{(\text{eq})}$ after $t \gtrsim 5P_c$. For models III and IV the amplitude of $D^{(\text{eq})}$ has been reduced so that the system is stable to $m = 1$. Therefore the linear growth of $D^{(\text{eq})}$ in models III and IV is the outcome of the violation of the center of mass condition.

We also show our equatorial and the meridional density snapshots throughout our integration in Figs. 6 and 7. The symmetry breaking of the bar structure occurs clearly at the time when the spiral arm forms in the equatorial snapshot and in the meridional plane. This becomes clear when we focus on the final snapshots of models I, II, and III.

We also in Fig. 8 show the diagnostics which contain both amplitude and phase. In order to make the picture clear, we first concentrate on the model III, the weakest dynamically unstable bar system of three models.

The behaviours in the diagnostics are clearly understood once we compute the spectra of the diagnostics (Fig. 9). From the spectra we find the following two remarkable issues. One is that the spectra $|F_1|^2$, $|F_2|^2$, $|F_3|^2$ take a peak around $\omega_{\text{bar}} \approx 5 \sim 6P_c^{-1}$ for models I, II, III, and the other is that $|F_3|^2$, $|F_4|^2$, $|F_z|^2$ take a peak around $\omega_{\text{quad}} \approx 2\omega_{\text{bar}} \approx 10 - 12P_c^{-1}$ for bar unstable stars. Combining the present feature with the behaviour of the five diagnostics explained before (Fig. 1), the dynamically unstable bar acts as follows.

Firstly the $m = 2$ mode grows and acts as a dominant mode of all because of the dynamical bar instabil-

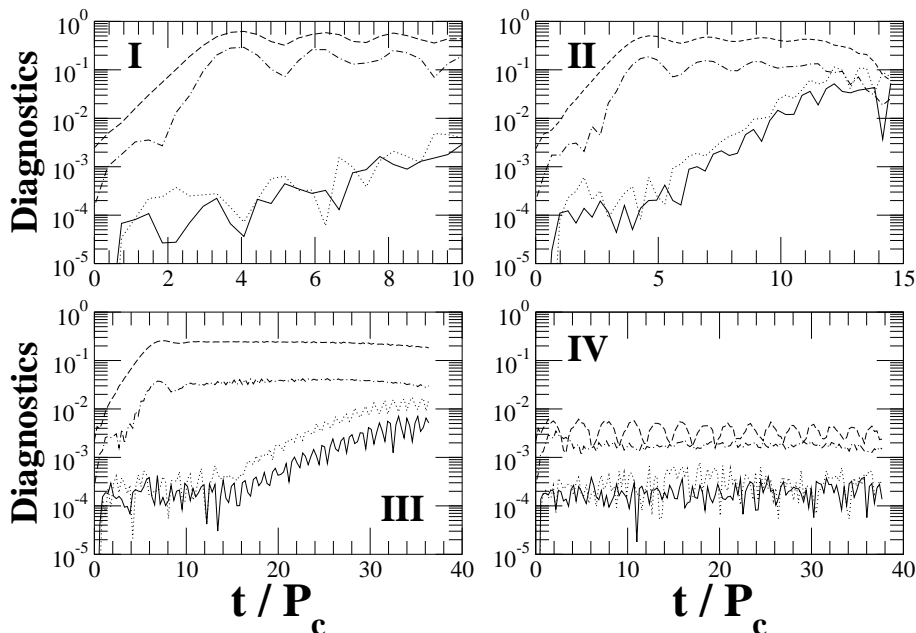


FIG. 5: Same as Fig. 4, but the center of mass is adjusted to zero in every snapshots.

ity. Next the $m = 4$ mode grows because of the secondary harmonic of the $m = 2$ mode. In fact the saturation amplitude of the $m = 4$ is approximately ≈ 0.3 for model I, 0.2 for model II, and 0.04 for model III, all of which are the order of the square of the saturation amplitude of the $m = 2$ ($\approx 0.6^2$ for model I, 0.5^2 for model II, 0.2^2 for model III). After that Faraday resonance occurs, which is clearly found in both D_z and $|F_z|^2$ from the fact $\omega_{\text{quad}} \approx 2\omega_{\text{bar}}$.

Note that Faraday resonance occurs in the fluid mechanics when the oscillation of the vertical direction is twice (2ω) as much as the one in the horizontal direction (ω) in the weakly nonlinear interaction [1, 30]. The reason why the resonance does not clearly appear in model I is either the strongly nonlinear effect or the insufficient duration time of quasi-periodic oscillation for computing the spectrum. Then, there is a resonance between $m = 1$ and $m = 2$, $m = 3$ and $m = 4$. The possibility of such resonances is three wave interaction: either $m = 1$ (ω_{bar}) and $m = 2$ (ω_{bar}) generates $m = 3$ ($\omega_{\text{bar}} + \omega_{\text{bar}}$) or $m = 3$ ($2\omega_{\text{bar}}$) and $m = 2$ (ω_{bar}) generates $m = 1$ ($2\omega_{\text{bar}} - \omega_{\text{bar}}$) in the dominant part. It is the fact found in the nonlinear behaviour of the dynamically unstable bar system.

The gravitational waveform and its spectrum have been computed by the quadrupole formula observed along the rotational axis and in the equatorial plane (Figs. 10 – 13). There are two remarkable features in gravitational waves from the viewpoint of nonlinear behaviour. One is that the quasi-periodic oscillation does not last until the radiation reaction timescale but decays because of the symmetry breaking of the dynamical bar. The duration period is related to the degree of nonlinearity of the bar mode instability, which is estimated from the inclination angle of the amplitude of the $m = 1$

($\text{Re}[D]$) and $m = 3$ ($\text{Re}[O]$) diagnostics. In the present case, the duration period of the bar structure is estimated as $\sim 10P_c$ for model I, $\sim 15P_c$ for model II, and $\sim 35P_c$ for model III. The other is that Faraday resonance has clearly appeared in the spectrum of gravitational waveform observed at least in the equatorial plane. Since we adopt quadrupole formula to compute gravitational waves, the higher order harmonics of the unstable bar mode such as $m = 4$ mode cannot be seen in this spectrum. Therefore a peak around $\omega \approx 12P_c^{-1}$ in Fig. 11 indicates the fact of an oscillation along the z -axis, which is the evidence of *Faraday resonance*. We have also computed the gravitational waveform and its spectrum observed along the z -axis and found that there is no peak around $\omega \approx 12P_c^{-1}$ in model III (Fig. 13). The fact also supports that a peak around $\omega \approx 12P_c^{-1}$ in Fig. 11 is the outcome of Faraday resonance, since an oscillation along z -direction can be clearly observed by gravitational waves in the equatorial plane, not in the rotation axis. When we increase the degree of nonlinearity, the above feature of the Faraday resonance in gravitational waves can be also seen in the equatorial plane.

IV. CONCLUSION

We investigate the nonlinear effects of dynamically bar unstable stars by means of three dimensional hydrodynamic simulations in Newtonian gravity. In order to follow the bar shape as long as possible, the initial amplitudes for odd azimuthal perturbations are significantly suppressed in our models.

We find interesting mode coupling in the dynamically unstable system in the nonlinear regime, and that only

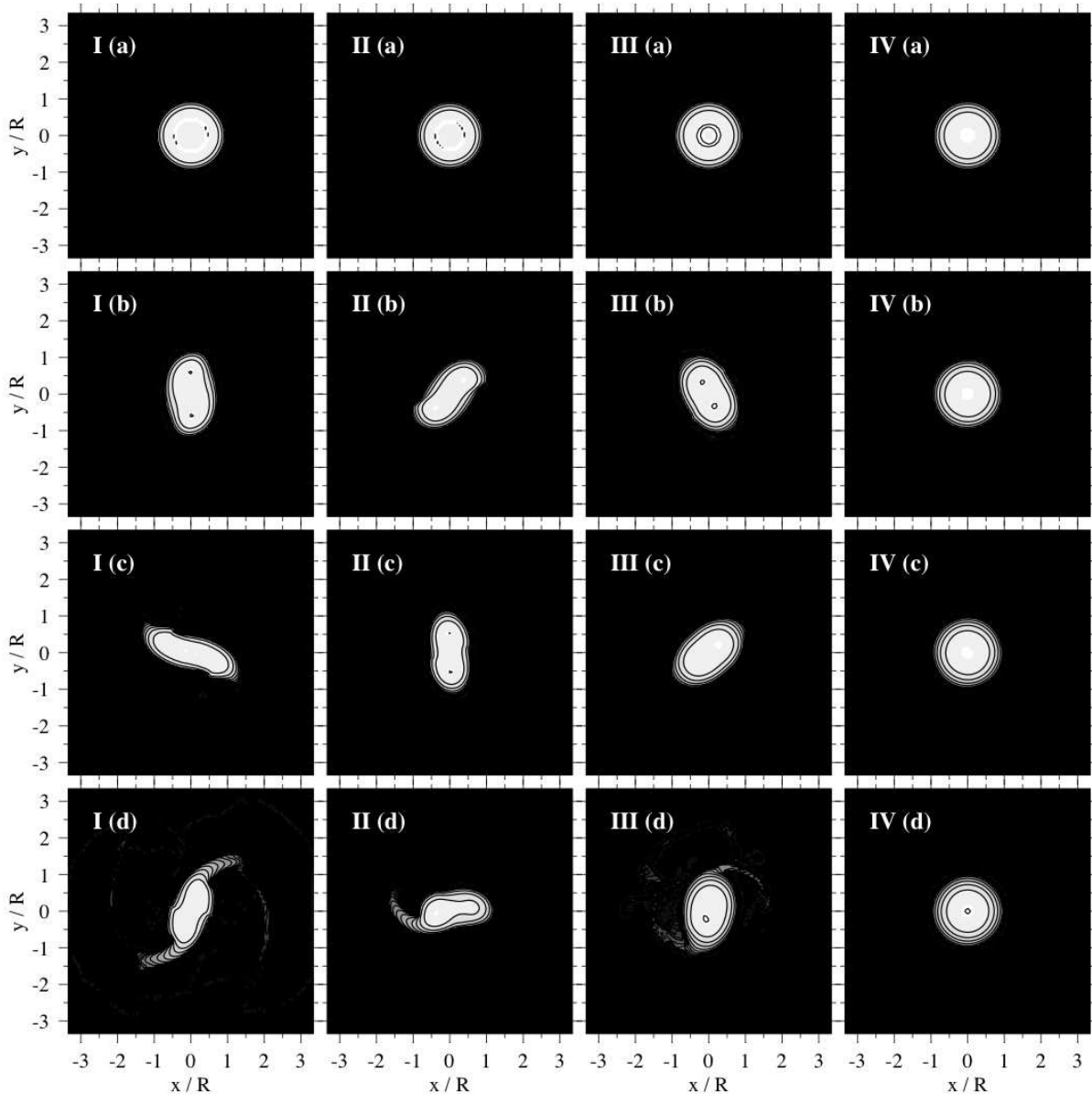


FIG. 6: Density contours in the equatorial plane throughout the evolution. Snapshots are plotted at $(t/P_c, \rho_{\max}/\rho_{\max}^{(0)}, d) = \text{I(a)} (3.70 \times 10^{-4}, 1.00, 0.25000)$, $\text{I(b)} (2.40, 1.21, 0.25000)$, $\text{I(c)} (5.92, 1.27, 0.25000)$, $\text{I(d)} (8.87, 1.46, 0.25000)$, $\text{II(a)} (3.29 \times 10^{-4}, 1.00, 0.20625)$, $\text{II(b)} (3.95, 1.20, 0.20625)$, $\text{II(c)} (7.90, 1.29, 0.20625)$, $\text{II(d)} (11.85, 1.58, 0.20625)$, $\text{III(a)} (2.98 \times 10^{-4}, 1.00, 0.25000)$, $\text{III(b)} (11.93, 1.13, 0.25000)$, $\text{III(c)} (23.85, 1.19, 0.25000)$, $\text{III(d)} (35.78, 1.27, 0.25000)$, $\text{IV(a)} (2.75 \times 10^{-4}, 1.00, 0.25000)$, $\text{IV(b)} (12.10, 1.05, 0.25000)$, $\text{IV(c)} (24.20, 1.10, 0.25000)$, $\text{IV(d)} (36.30, 1.16, 0.25000)$, where ρ_{\max} is the maximum rest mass density and $\rho_{\max}^{(0)}$ is the maximum rest mass density at $t = 0$. The contour line denotes $\rho/\rho_{\max} = 10^{(16-i)d}$ ($i = 1, \dots, 15$). Hereafter R denotes the equatorial radius at $t = 0$.

before the destruction of the bar. The quasi-periodic oscillation mainly along the rotational axis is induced. The characteristic frequency is twice as big as that of the dynamically unstable bar mode. This feature is quite analogous to the Faraday resonance. Although our finding is only supported by the weakly nonlinear theory of fluid mechanics, we have also found the same feature of parametric resonance even in the strongly nonlinear regime. There is one qualitative difference between Faraday res-

onance and our numerical result. Faraday resonance has lower frequency than that of the forced oscillation, while our result has higher frequency than that of the bar unstable mode. The fact can be understood by the different regime of the media. Since the media of the rotating star is a perfect fluid, which is only contained inside the star, there should be a cutoff frequency to be amplified. In fact, introducing a cutoff frequency with a polar radius of the star and the sound speed computed by the

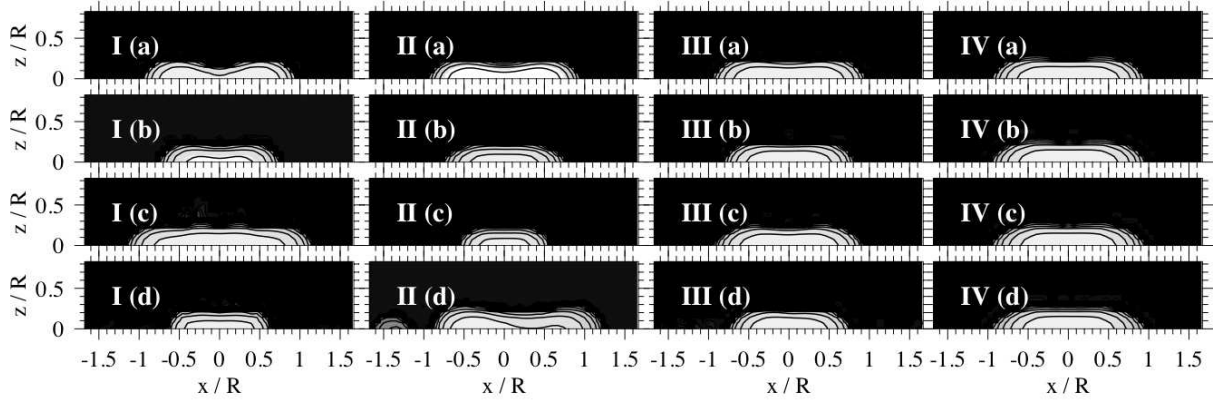


FIG. 7: Same as Fig. 6 but in the meridional plane.

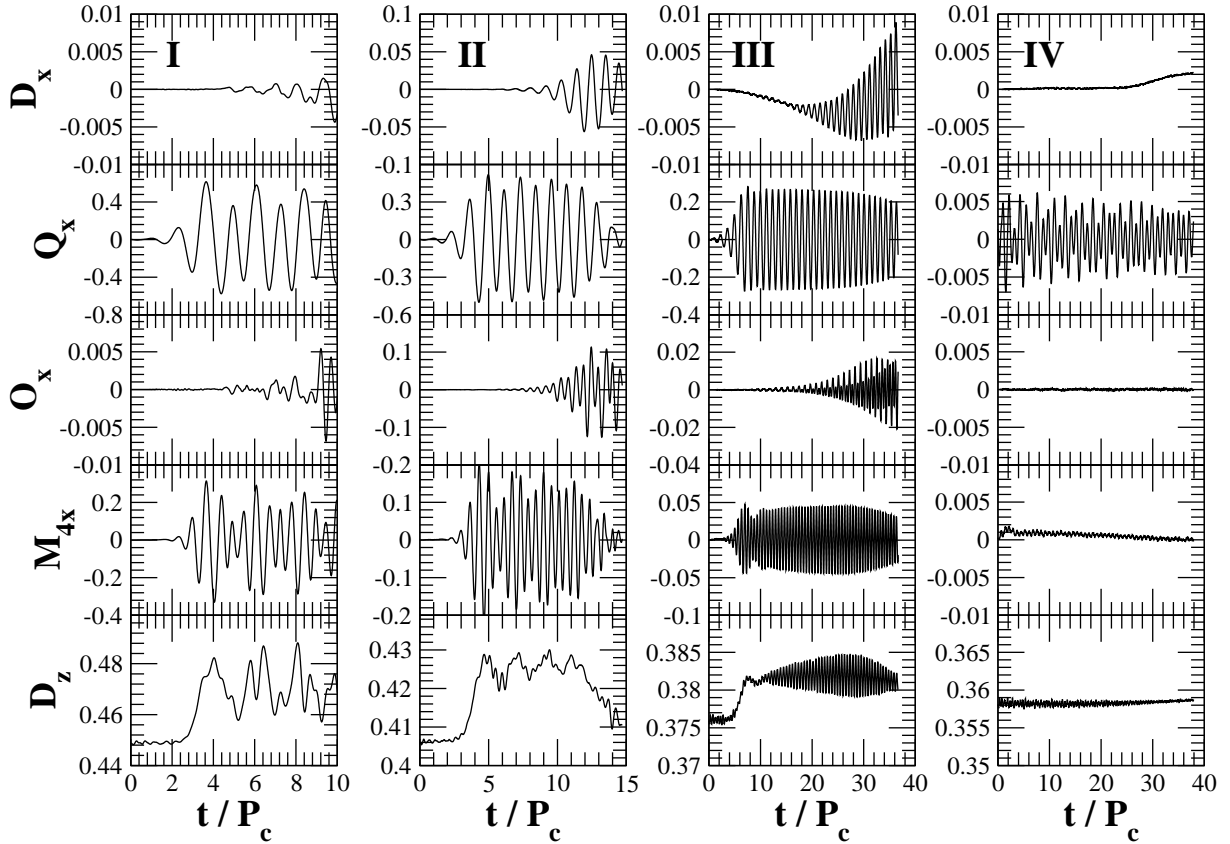


FIG. 8: Diagnostics $\Re[D]$, $\Re[Q]$, $\Re[O]$, $\Re[M_4]$, and D_z as a function of t/P_c for four different rotating stars (see Table I).

mean density, the cutoff frequency ω_{cut} is estimated as $\omega_{\text{cut}} \approx \omega_{\text{bar}}$. Therefore a higher frequency than the bar is amplified. The fact also indicates that our finding is interpreted as a parametric resonance.

We also discuss the detectability of Faraday resonance by gravitational waves. The characteristic frequency and the amplitude of gravitational waves can be estimated as

$$f_{\text{bar}} \sim 2 \left(\frac{10 \text{ km}}{R} \right) \left(\frac{T/W}{0.25} \right)^{1/2} \left(\frac{M/R}{0.15} \right)^{1/2} [\text{kHz}], \quad (4.1)$$

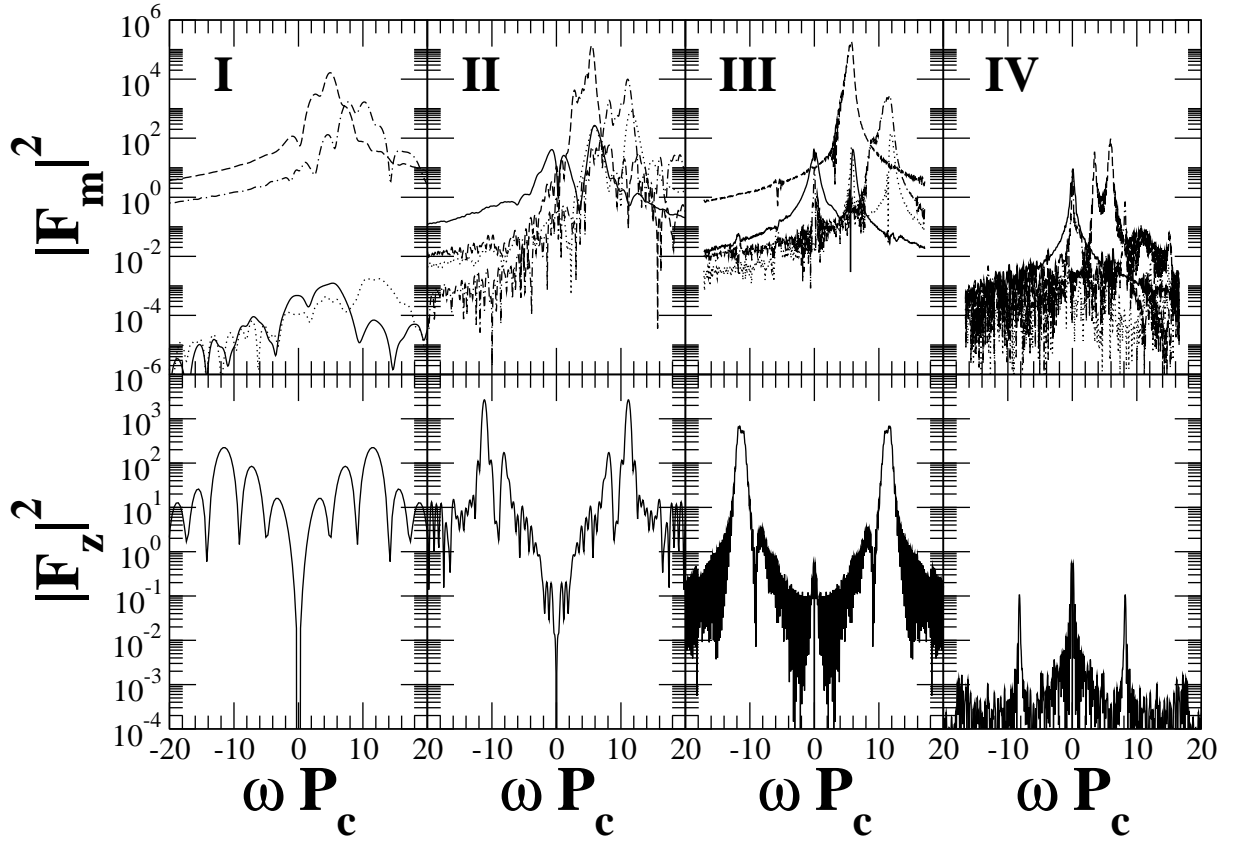


FIG. 9: Spectra $|F_m|^2$ and $|F_z|^2$ as a function of ωP_c for four different rotating stars (see Table I). Solid, dashed, dotted, and dash-dotted line of $|F_m|^2$ denote the values of $m = 1, 2, 3,$ and $4,$ respectively.

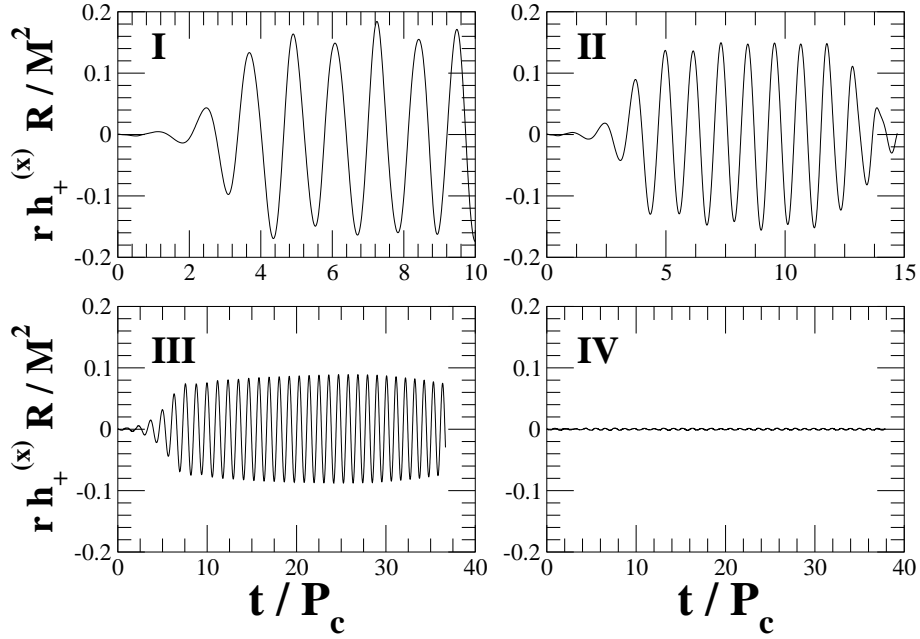


FIG. 10: Gravitational waveform (+ mode) observed at the x axes for four different rotating stars (See Table I). Note that \times mode is identically zero because we adopt the equatorial symmetry.

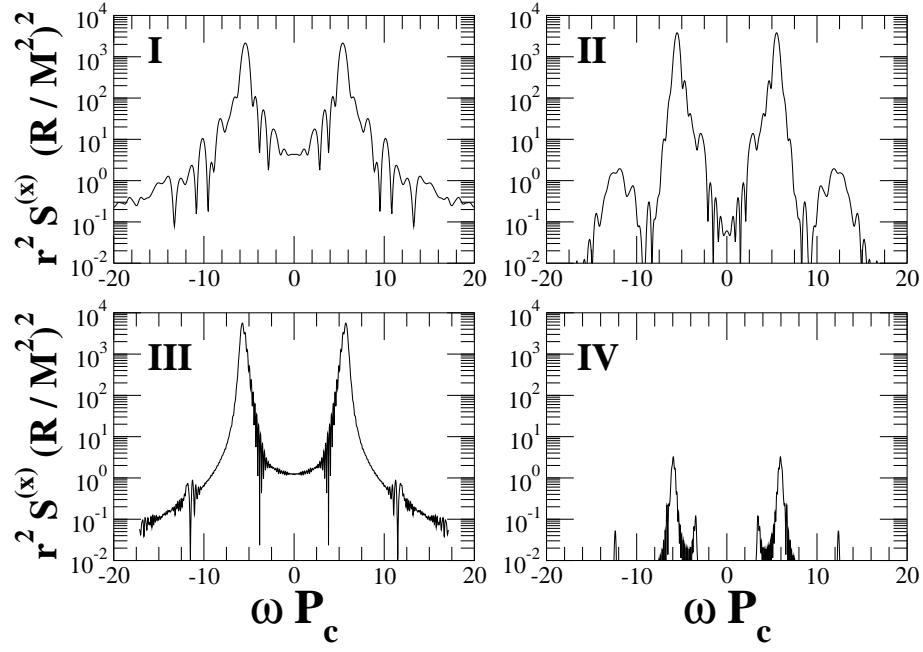


FIG. 11: Spectra of gravitational waveform (+ mode) observed at the x axes for four different rotating stars (See Table I).

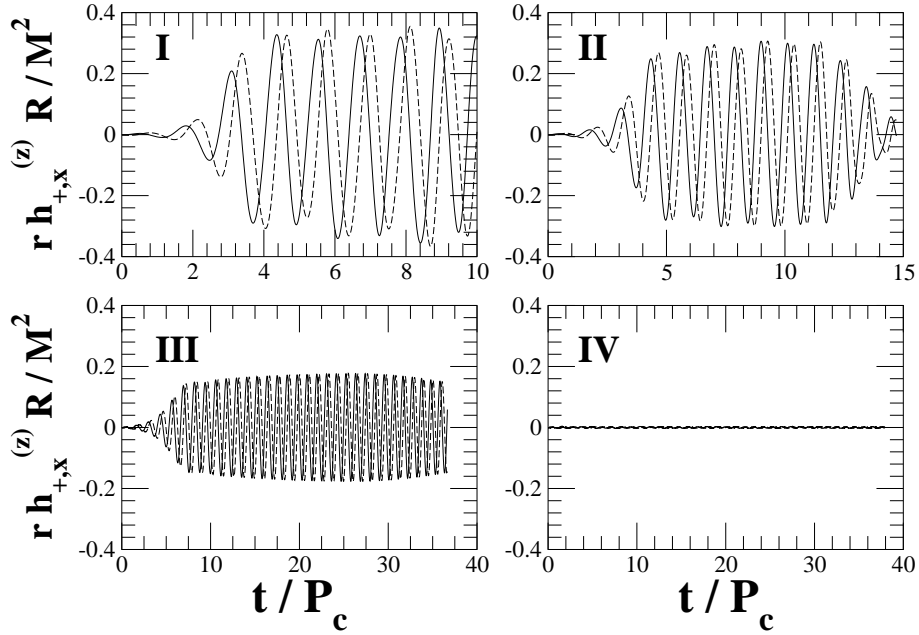


FIG. 12: Gravitational waveform observed at the z axes for four different rotating stars (See Table I). Solid and dashed line denotes + mode and \times mode, respectively.

$$h_{\text{bar}} \sim 2 \times 10^{-23} \left(\frac{M}{1.4M_{\odot}} \right) \left(\frac{20\text{Mpc}}{d_{\text{obs}}} \right) \left(\frac{M/R}{0.15} \right) \left(\frac{T/W}{0.25} \right), \quad (4.2)$$

where d_{obs} is the distance from the observer. If the bar formation occurs in Virgo cluster, quasi-periodic waveform can be detected in the second generation of gravitational wave detectors such as Advanced LIGO, Ad-

vanced Virgo, and Large-scale Cryogenic Gravitational wave Telescope (LCGT), or in the third generation European Gravitational Wave Observatory. The frequency of the parametric resonance is around twice as big of that

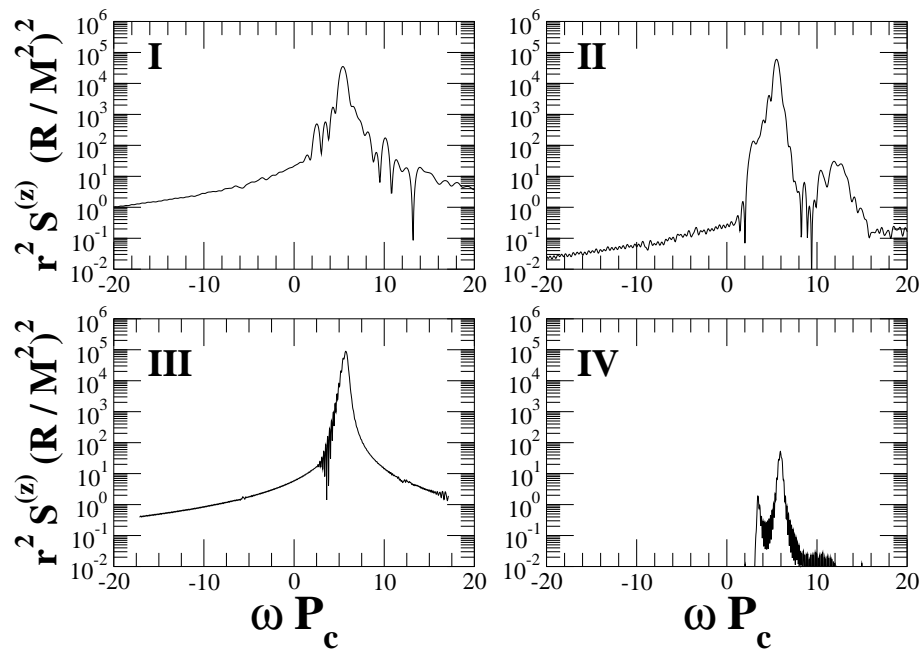


FIG. 13: Spectra of gravitational waveform observed at the z axes for four different rotating stars (See Table I).

of the bar unstable mode, and the amplitude of the parametric resonance is roughly two orders lower ($\approx 1\%$) than that of bar unstable mode. The detection of gravitational waves from parametric resonance may explore the non-linear phase of the dynamically bar unstable stars such as determining the saturation amplitude of gravitational waveform from the bar unstable system, parametric resonance, and the duration period of the bar structure.

Acknowledgments

MS thanks Nils Andersson, Silvano Bonazzola, Brandon Carter, Pablo Cerda-Duran, Eric Gourgoulhon,

Kei Kotake, Ewald Müller, Luciano Rezzolla, Shin Yoshida for discussion. MS also thanks Misao Sasaki for his kind hospitality at the Yukawa Institute for Theoretical Physics, where part of this work was done. This work was supported in part by the STFC rolling grant (No. PP/E001025/1), by the PPARC grant (No. PPA/G/S/2002/00531) at the University of Southampton, and by the Grant-in-Aid for the 21st Century Center of Excellence in Physics at Kyoto University. Numerical computations were performed on the myrinet nodes of Iridis compute cluster in the University of Southampton, and on the SGI-Altix3700 in the Yukawa Institute for Theoretical Physics, Kyoto University.

-
- [1] J. Miles and D. Hederson, *Ann. Rev. Fluid Mech.* **22**, 143 (1990).
[2] O. Ben-David, M. Assaf, J. Fineberg, and B. Meerson, *Phys. Rev. Lett.* **96**, 154503 (2006).
[3] P. Engels, C. Atherton, and M. A. Hofer, *Phys. Rev. Lett.* **98**, 095301 (2007).
[4] S. Chandrasekhar, *Ellipsoidal Figures of Equilibrium*, (Yale Univ. Press, New York, 1969), Chap. 5.
[5] J. E. Tohline, R. H. Durisen, and M. McCollough, *Astrophys. J.* **298**, 220 (1985).
[6] R. H. Durisen, R. A. Gingold, J. E. Tohline, and A. P. Boss, *Astrophys. J.* **305**, 281 (1986).
[7] H. A. Williams and J. E. Tohline, *Astrophys. J.* **334**, 449 (1988).
[8] J. L. Houser, J. M. Centrella, and S. C. Smith, *Phys. Rev. Lett.* **72**, 1314 (1994).
[9] S. C. Smith, J. L. Houser, and J. M. Centrella, *Astrophys. J.* **458**, 236 (1995).
[10] J. L. Houser and J. M. Centrella, *Phys. Rev. D* **54**, 7278 (1996).
[11] J. Toman, J. N. Imamura, B. J. Pickett, and R. H. Durisen, *Astrophys. J.* **497**, 370 (1998).
[12] K. C. B. New, J. M. Centrella, and J. E. Tohline, *Phys. Rev. D* **62**, 064019 (2000).
[13] Y. -T. Liu and L. Lindblom, *Mon. Not. R. Astron. Soc.* **324**, 1063 (2001).
[14] Y. -T. Liu, *Phys. Rev. D* **65**, 124003 (2002).
[15] J. E. Tohline and I. Hachisu, *Astrophys. J.* **361**, 394 (1990).
[16] B. K. Pickett, R. H. Durisen and G. A. Davis, *Astrophys. J.* **458**, 714 (1996).
[17] M. Shibata, S. Karino, and Y. Eriguchi, *Mon. Not. R. Astron. Soc.* **334**, L27 (2002); **343**, 619 (2003).
[18] M. Shibata, T. W. Baumgarte, and S. L. Shapiro, *Astro-*

- phys. J. **542**, 453 (2000).
- [19] M. Saijo, M. Shibata, T. W. Baumgarte, and S. L. Shapiro, *Astrophys. J.* **548**, 919 (2001).
- [20] L. Baiotti, R. De Pietri, G. M. Manca, and L. Rezzolla, *Phys. Rev. D* **75**, 044023 (2007).
- [21] S. Ou, J. E. Tohline, and P. M. Motl, *Astrophys. J.* **665**, 1074 (2007).
- [22] J. M. Centrella, K. C. B. New, L. L. Lowe, and J. D. Brown, *Astrophys. J.* **550**, L193 (2001).
- [23] M. Saijo, T. W. Baumgarte, S. L. Shapiro, *Astrophys. J.* **595**, 352 (2003).
- [24] S. Ou and J. E. Tohline, *Astrophys. J.* **651**, 1068 (2006).
- [25] P. Cerda-Duran, V. Quilis, J. A. Font, *Comp. Phys. Comm.* **177**, 288 (2007).
- [26] A. L. Watts, N. Andersson, D. I. Jones, *Astrophys. J.* **618**, L37 (2005).
- [27] M. Saijo and S. I. Yoshida, *Mon. Not. R. Astron. Soc.* **368**, 1429 (2006).
- [28] J. -L. Tassoul, *Theory of Rotating Stars* (Princeton Univ. Press., Princeton, 1978), Chap. 10.
- [29] S. L. Shapiro and S. A. Teukolsky, *Black Holes, White Dwarfs, and Neutron Stars* (John Wiley and Sons, New York, 1983), Chap. 7.5.
- [30] P. G. Drazin and W. H. Reid, *Hydrodynamic Stability* (Cambridge Univ. Press., Cambridge, 1981), Sec. 48.
- [31] J. D. Brown, in *Astrophysical Sources for Ground-based Gravitational Wave Detectors*, edited by J. M. Centrella (American Institute of Physics, New York, 2001), 234.
- [32] R. D. Richtmyer and K. W. Morton, *Difference Methods for Initial Value Problem* (Krieger, Florida, 1994), 313
- [33] I. Hachisu, *Astrophys. J. Suppl.* , 61, 479 (1986).
- [34] C. W. Misner, K. S. Thorne, and J. A. Wheeler, *Gravitation* (Freeman, New York, 1973)
- [35] L. S. Finn, in *Frontiers in Numerical Relativity*, edited by C. R. Evans, L. S. Finn, and D. W. Hobill (Cambridge Univ. Press, Cambridge, 1989), 126.
- [36] The speed of light only enters through the quadrupole formula of gravitational waves.
- [37] The numerical finite difference error is in principle sufficient to trigger instabilities, but starting from such a small amplitude it would take the instability significantly long to reach saturation.